JACS
JOURNAL OF THE AMERICAN CHEMICAL SOCIETY
Article
Cite This: J. Am. Chem. Soc. 2018, 140, 13441−13448
pubs.acs.org/JACS

Understanding the Behavior of the Above-Room-Temperature Molecular Ferroelectric 5,6-Dichloro-2-methylbenzimidazole Using Symmetry Adapted Distortion Mode Analysis

Huiyu Liu,[†] Weiguo Zhang,[‡] P. Shiv Halasyamani,[‡] Harold T. Stokes,[§] Branton J. Campbell,[§] John S. O. Evans,*[,†] and Ivana Radosavljevic Evans*[,†]

[†]Department of Chemistry, Durham University, Science Site, Durham DH1 3LE, United Kingdom
[‡]Department of Chemistry, University of Houston, Houston, Texas 77204-5003, United States
[§]Department of Physics & Astronomy, Brigham Young University, Provo, Utah 84602, United States

Supporting Information

ABSTRACT: The exploitable properties of many functional materials are intimately linked with symmetry-changing phase transitions. These include properties such as ferroelectricity, second harmonic generation, conductivity, magnetism and many others. We describe a new symmetry-inspired method for systematic and exhaustive evaluation of the symmetry changes possible in molecular systems using molecular distortion modes, and how different models can be automatically tested against diffraction data. The method produces a quantitative structural landscape from which the most appropriate structural description of a child phase can be chosen. It can be applied to any molecular or molecular-fragment containing material where a (semi) rigid molecule description is appropriate. We exemplify the method on 5,6-dichloro-2-methylbenzimidazole (DC-MBI), an important molecular ferroelectric. We show that DC-MBI undergoes an unusual symmetry-lowering transition on warming from orthorhombic $Pca2_1$ ($T \lesssim 400$ K) to monoclinic *Pc*. Contrary to expectations, the high temperature phase of DC-MBI remains polar.

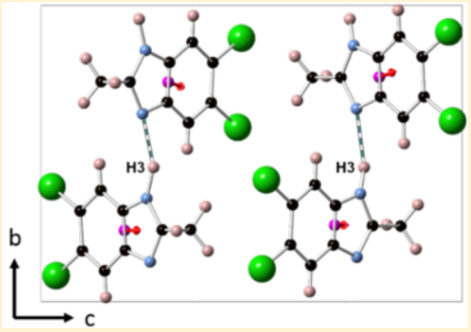

INTRODUCTION

Ferroelectricity has long been an important topic in solid state and materials chemistry. It is associated with a variety of technological applications such as memories, modulators, and energy harvesting devices.[1,2] Extensively studied ferroelectrics include inorganic materials such as $BaTiO_3$,[3,4] $PbTiO_3$,[5−8] PZT,[9−12] KDP and similar,[13−19] KTP[20−24] and Rochelle salt.[25−29] In recent years there has been significant interest in organic ferroelectrics which offer the advantages of being lightweight, flexible and nontoxic. Potential applications include actuators, transducers and pyroelectric detectors, as a result of their excellent dielectric, pyro- and piezo-electric properties comparable to traditional inorganic ferroelectrics.[30−33] Molecular systems such as chloranilic acid phenazine[34−37] and croconic acid[33,38−40] have been reported to exhibit ferroelectricity near room temperature.

The single-component hydrogen-bonded material, 5,6-dichloro-2-methylbenzimidazole (DC-MBI, Figure 1), has been reported to exhibit ferroelectricity above room temperature.[41] The room-temperature form of DC-MBI is orthorhombic and polar (space group $Pca2_1$) and the ferroelectricity is thought to arise from the positional ordering of protons along chains of N−H···N hydrogen bonds (involving H3 of Figure 1). The material was reported to retain ferroelectricity at 373 K, above which (~400 K) a phase transition was reported based on DSC data. No details of the high temperature structure were reported, though the presence of strong pseudosymmetry in the ferroelectric polar structure, suggested the existence of a potential paraelectric centrosymmetric high-temperature structure. In fact disordering of the H3 protons in the N−H3···N hydrogen bond chain (Figure 3a) would introduce an additional mirror plane in the molecule, raising the symmetry to *Pbcm*, and would provide

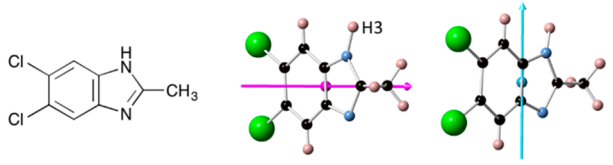

Figure 1. Left: molecular structure of 5,6-dichloro-2-methylbenzimidazole (DC-MBI). Right: examples of axial vectors describing symmetry adapted molecular rotation modes. The rotation vector passes through a pivot point (colored sphere); its direction identifies the rotation axis while its length is proportional to the rotation angle (see text). The pink vector corresponds to modes *r*5 and *r*6 of irrep Γ_4^+ (discussed later in the paper) with *r*6 = −*r*5; the blue vector describes a mode of irrep Γ_3^-.

Received: August 10, 2018
Published: September 19, 2018

DOI: 10.1021/jacs.8b08591
J. Am. Chem. Soc. 2018, 140, 13441−13448

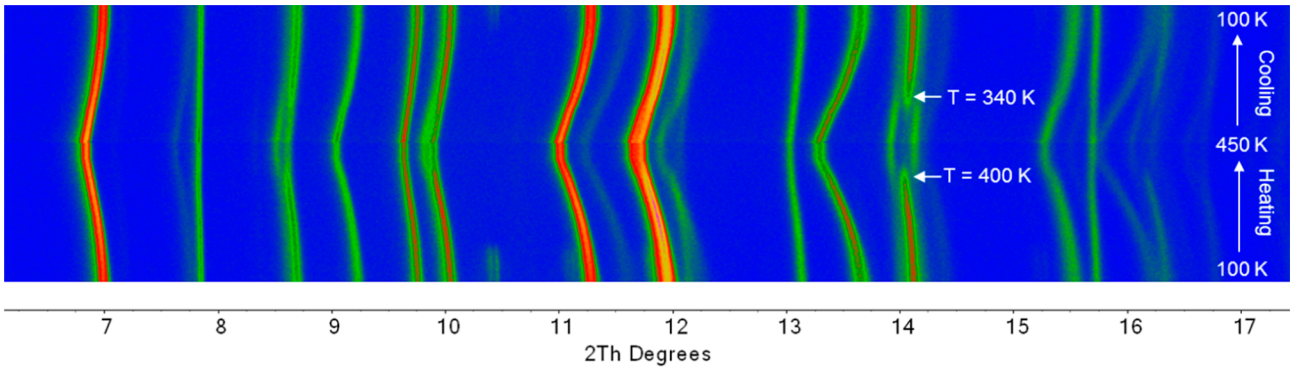

Figure 2. Variable-temperature laboratory PXRD patterns on warming and cooling between 100 and 450 K. Artificial color map shows intensity changes on heating and cooling.

an obvious ferroelectric switching mechanism, as proposed in previous work.

Here we present evidence that DC-MBI does indeed undergo a reversible phase transition, but we demonstrate an unusual and rather surprising lowering of the space-group symmetry upon heating to another polar phase. We describe the use of molecular symmetry adapted distortion modes to systematically derive and explore all possible patterns of molecular DC-MBI rotations and displacements consistent with the experimentally determined unit cell size. Each candidate structure was tested against variable temperature powder X-ray diffraction (PXRD) data in order to solve the structure of the HT phase in a systematic, exhaustive, and automated fashion. We also show how molecule distortion modes[42] offer a remarkably convenient low-parameter-number description of the phase transition. We discuss the implications of the phase transition for ferroelectric switching. This is the first time molecular distortion modes have been used to determine the structure of a functional molecular material from diffraction data. The general approach we have developed and adopted here will be widely applicable to phase transitions in any molecular material or any structure incorporating molecular fragments such as metal organic frameworks (MOFs).

EXPERIMENTAL SECTION

Sample Preparation. 5,6-Dichloro-2-methylbenzimidazole (DC-MBI) was purchased from Sigma-Aldrich. For powder diffraction experiments and second harmonic generation measurements, the material was used as-purchased. Single crystals of DC-MBI (0.0201 g) were prepared by slow evaporation of an alcohol (methanol or ethanol) solution (typically 3 mL) at room temperature. Colorless needle-shaped crystals appeared after 1 week.

Laboratory and Synchrotron X-ray Diffraction. Variable-temperature powder diffraction data were collected on two different Bruker D8 Advance instruments. High-temperature data were collected in capillary mode on a Mo Kα diffractometer equipped with a Lynx-Eye detector and an Oxford Cryosystems Cryostream Plus device. Gently ground sample was loaded into a 0.7 mm borosilicate glass capillary, mounted on the goniometer head and rotated during data collection. A small amount of Al powder was added to DC-MBI for temperature calibration. The sample was cooled from 450 to 100 K at a rate of 15 K h^{-1}, and then was warmed from 100 K back to 450 K at the same rate. A series of 20 min PXRD patterns were recorded over the 2θ range 2°−30° using a step size of 0.02°. Lower-temperature data were collected in flat-plate mode, on a Cu K$\alpha_{1,2}$ diffractometer equipped with a Lynx-Eye detector and Oxford Cryosystem PheniX closed-circuit cryostat. For this experiment, a gently ground sample was mixed with Al and Si powders (as internal standards) and placed onto a silicon flat plate. The sample was cooled from room temperature to 12 K at a rate of 15 K h^{-1}. The data were collected over a 2θ range of 5°−70° using a step size of 0.02°.

Synchrotron powder X-ray diffraction data were collected on beamline I11 of the Diamond Light Source in high-resolution mode using the 45 Multi-Analyzing Crystal (MAC) detectors. Samples were placed into a 0.7 mm quartz capillary attached to a brass holder which was spun during the measurement. Both 100 and 500 K data were collected for 2h using λ = 0.8257653 Å (calibrated against silicon standard NIST 640c). All powder diffraction data were analyzed using Topas Academic software.[43,44]

Single crystals were screened and measured using a Bruker SMART 6000 equipped with a CCD area detector and an Oxford Cryosystems Nitrogen Cryostream 600 cryostat.

Second Harmonic Generation (SHG) Measurement. Approximately 0.10 g of polycrystalline DC-MBI was placed in a 0.50 mm diameter fused silica tube and heated in a home-built sample holder equipped with a hot plate and a thermometer. α-SiO_2 was used as a reference. The SHG measurement system has been described previously.[45]

Exhaustive Symmetry Approach. An exhaustive tree of intermediate subgroups that lie between a hypothetical *Pbcm* parent structure and a *P*1-symmetry base structure with the same primitive unit cell size was calculated using the ISODISTORT software. Molecular rigid bodies were defined in *P*1 symmetry, with a pivot point located at the midpoint of the C−C bond shared by both rings (Figure 1). An input file for analysis was automatically prepared by ISODISTORT containing rotational distortion modes that assign rotation vectors to each of the molecular pivots in the unit cell. Modes were automatically flagged to refine or remain fixed according to their irreducible representation to describe each space group of the candidates in Figure 4. For each candidate the model was then refined against high-temperature synchrotron powder data. Several thousand cycles of refinement followed by randomization of mode amplitudes and cell parameters and rerefinement were performed for each candidate.

RESULTS AND DISCUSSION

Observation of a Structural Phase Transition in DC-MBI. Our initial attempts to investigate the high-temperature structure of DC-MBI employed single crystal X-ray diffraction. Several crystals of different sizes were tested. They initially diffracted well during heating from room temperature, but shattered at 450 K, presumably due to an abrupt volume change, suggesting a first-order phase transition.

Laboratory variable-temperature PXRD patterns (Figure 2) were therefore collected on both warming and cooling between 100 and 450 K. It is apparent that the material undergoes a reversible phase transition. All peaks shift in a smooth fashion

DOI: 10.1021/jacs.8b08591
J. Am. Chem. Soc. 2018, 140, 13441−13448

as the temperature increases until the phase transition ($T_c \sim$ 400 K for warming and $T_c \sim$ 340 K for cooling) takes place. At high temperature, some peaks appear to split, indicating a surprising loss of symmetry relative to the low-temperature phase. The observation of a temperature hysteresis in the peak splitting is again consistent with a first-order phase transition.

Crystal Structure of the LT Phase of DC-MBI. The structure of the low-temperature (LT) phase of DC-MBI has been reported previously (at 295 K),[41] but was redetermined in this work at 120 K via single crystal X-ray diffraction to allow comparison with the new high-temperature structure. The fractional coordinates of all atoms were refined freely; anisotropic atomic displacement parameters (ADPs) were refined for the non-hydrogen atoms, while the hydrogen atoms were refined isotropically. An *R*-factor of 2.7% was obtained. At 120 K, the material has cell parameters of a = 13.9343(3) Å, b = 5.64024(15) Å, c = 10.3593(3) Å, V = 814.16(2) Å and retains the room-temperature $Pca2_1$ structure. Figure 3b shows

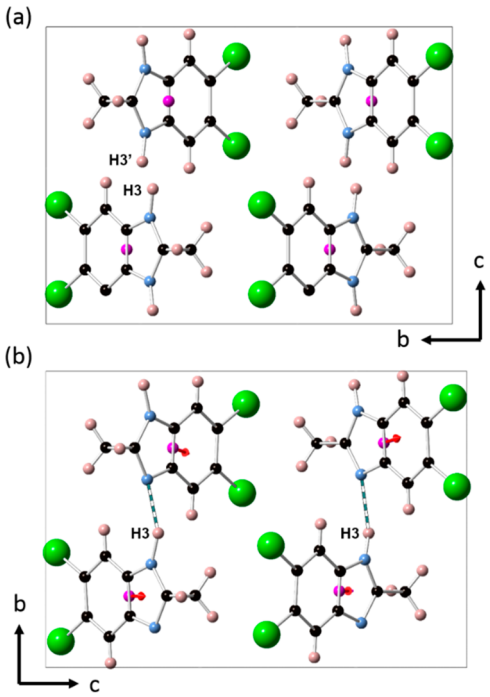

Figure 3. Crystal structures of DC-MBI view down the crystallographic *a*-axis. (a) Crystal structure of hypothetical high-symmetry parent in which proton disorder over H3 and H3′ leads to space group *Pbcm*. (b) Crystal structure of low-symmetry HT child. The overall rotation vectors (discussed later in the text) are depicted in pink. Cell axes correspond to the symmetry modes description used in the structure solution process and in later figures.

the hydrogen bonding pattern of the LT phase (essentially identical to that of the HT phase, as shown below). DC-MBI molecules connect via intermolecular N−H3···N hydrogen bonds, forming infinite chains that stack along the crystallographic *b*-axis. The polarity of each hydrogen-bonded chain is directed along the crystallographic *c*-axis (in the $Pca2_1$ standard setting). The bond distances involved in the N−H3···N hydrogen bond are d(N1···N2) = 2.962(3) Å and d(N1−H3) = 0.847(25) Å.

Structure Solution of HT Phase: Exhaustive Symmetry Mode Subgroup Search. It is clear from inspection of the powder diffraction data in Figure 2 that the HT phase of DC-MBI is closely related to the LT phase. However, the peak splitting demonstrates that it has lower metric symmetry and therefore cannot be the putative *Pbcm* proton-disordered centrosymmetric structure proposed in earlier work. In fact, the HT data can be successfully indexed using a monoclinic cell with a = 10.3812 Å, b = 14.487 Å, c = 5.7383 Å and β = 90.950 Å. As is typical of powder diffraction experiments, it is hard distinguish between the candidate space group type for the HT phase based on systematic absences alone.

Solving pseudosymmetric structures from powder diffraction data is a significant challenge, and there are numerous examples in the literature where structures have been revised multiple times due to incorrect unit cell or space group choices, particularly for functional inorganic materials. Recently, a variety of exhaustive methods for overcoming these problems have been described based on isotropy subgroups and symmetry-adapted distortion modes.[46] In essence, these methods allow one to systematically and automatically construct and test a model for every intermediate subgroup between a high-symmetry parent structure and a lowest-possible-symmetry base structure, giving a quantitative global view of the structural landscape. In such an analysis, instead of the traditional parameter set of individual atomic *xyz* displacements, one quantifies a phase transition (i.e., deviations from the parent symmetry) in terms of mode amplitudes, where each symmetry-adapted mode belongs to some irreducible representation of the parent symmetry group and defines a global displacement pattern that affects many atoms or molecules. The advantages of the symmetry-mode parameter set have been discussed elsewhere.[39,46−50]

A further simplification of the parameter set that lends itself to molecular systems is the combined use of rotational and translational symmetry modes to describe the coherent motions of entire (semi) rigid-body units.[51] This overcomes the need to refine parameters describing individual atomic shifts, which would be beyond the information content of powder data for complex molecules. In this approach, an axial vector (pseudo vector) is "attached" to each molecule at a central pivot point (Figure 1), such that its direction indicates the direction of a right-handed molecular rotation while its magnitude indicates the rotation angle. The properties of this vector, which can be directly refined from diffraction data, encode the same information as a conventional rigid body description (up to 3 positions and 3 angles of rotation) but lend themselves to a symmetry-based description. In fact, rotational order parameters and symmetries are highly analogous to those of magnetic moments at magnetic ordering transitions, except that the magnetic time-reversal operation is not relevant to static molecules so that the resulting subgroups will naturally be restricted to one of the 230 crystallographic space groups (monochromatic or type-1 Shubnikov groups). The rotational symmetry-mode description has several practical advantages over a conventional rigid-body description: it is naturally defined relative to a reference structure (the parent) for which all rotations are zero; pivot-rotation vectors provide a clean graphical representation of the distortions occurring; and it is free of the order-of-operation subtleties involving noncommutative rotation matrices.

Because HT DC-MBI appears to have lower symmetry than the LT phase, we could use the LT phase as a parent structure from which to explore possible HT child structures. However, if we ignore the N−H3 proton, we can instead use the hypothetical high symmetry *Pbcm* structure as a parent of both

DOI: 10.1021/jacs.8b08591
J. Am. Chem. Soc. 2018, 140, 13441−13448

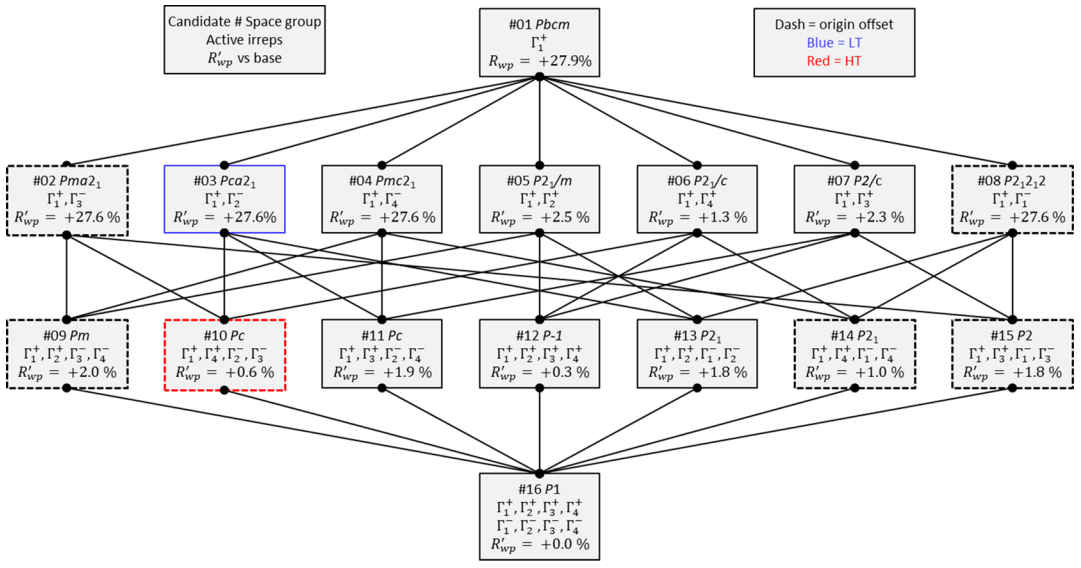

Figure 4. Tree of intermediate subgroups that lie between the symmetry groups of the hypothetical *Pbcm* parent structure and the *P*1 base structure. Active irreps are listed for each candidate in the tree along with the background-subtracted *R*-factor relative to the base (see text). LT space group shown with blue and HT with red border. Dashed border indicates an origin shift relative to the parent.

phases (Figure 3a). Using ISODISTORT, we calculated a tree of all intermediate subgroups that lie between the *Pbcm* parent structure and a *P*1−symmetry base structure, as shown in Figure 4. Because the PXRD data give no evidence for any increase in the size of the unit cell, this base structure is the lowest-possible subgroup that we need to consider. Note that some space group types (*Pc* and $P2_1$) appear multiple times with different origin shifts (relative to the parent) leading to distinct isotropy subgroups with inequivalent structural degrees of freedom.

Each of the candidate child structures was described in terms of the rotational and translational symmetry modes of the DC-MBI rigid-body allowed by the corresponding child subgroup, and Rietveld refinement was performed on each candidate against the HT diffraction data. For each candidate, we performed multiple cycles of refinement of both mode amplitudes and cell parameters, with values randomized after each convergence. The number of structural degrees of freedom ranged from 3 in space group *Pbcm* (one molecule with one rotational mode and 2 translational modes allowed by symmetry) to 24 in space group *P*1 (4 molecules with 3 rotational and 3 translational modes for each, though 3 translational degrees of freedom are set to zero to fix the origin in *P*1). The quality of fit found in each subgroup is included in Figure 4 as ΔR_{wp}, where ΔR_{wp} is the increase in R_{wp} over the lowest R_{wp} found in any subgroup. *R*-factors are also shown graphically in Figure 5, where we see identical trends with either R_{Bragg} or a background-subtracted-R_{wp}' as the quality indicator. The minimum R_{wp} was found multiple times during the annealing process, suggesting that proper convergence was achieved in each subgroup.

The lowest R_{wp} (2.5%) was found, as expected, for the base candidate #16 in space group *P*1. This description possesses all of the degrees of freedom of all its supergroups, plus sufficient flexibility that its cell metric can deviate from expected monoclinic values ($\alpha = \beta = 90°$ and $\gamma \neq 90°$ in the setting used). We note that α and β remained within ±0.005° of 90° in the best solution with γ refining to 91.2°. Subgroup #12 ($P\bar{1}$) gives the next best fit, though this candidate can be

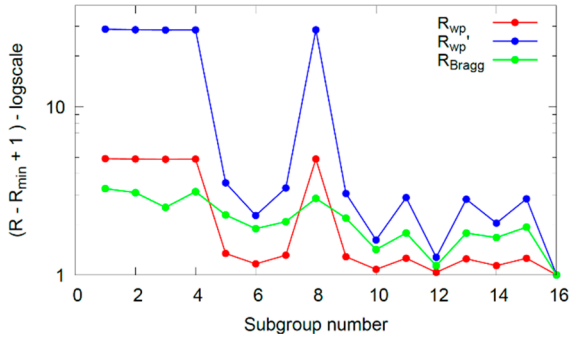

Figure 5. Three types of *R*-factor are presented for each candidate subgroup from fits to the HT data. Subgroups #1−#4 and #8 are orthorhombic; subgroups #12 and #16 are triclinic; the other subgroups are monoclinic. Data are plotted as $(R - R_{\#16} + 1)$ to enable the use of a log scale.

eliminated from the observation of a positive SHG signal up to melting. Of the monoclinic candidates (#5−#7, #9−#11, #13−#15), we find that candidate #10 (*Pc*) gives the best fit to the data with R_{wp} only marginally higher than that of #1 (*P*1), despite having far fewer degrees of freedom. We therefore select this candidate as having the optimum balance between giving an excellent fit to the data and having a low number of structural degrees of freedom. The final Rietveld fit for this candidate is shown in Figure 6, and the corresponding refined parameters are summarized in Table 1. The fit for the next-best monoclinic candidate (#11 *Pc*) is significantly worse, as shown in Figure S1 of the Supporting Information. Given the experimental observation of peak splitting, we could have excluded orthorhombic space groups (#1−#4 and #8) from our analysis. However, in cases with more subtle splitting, they would need to be included, so we retained them for completeness. As such, our process of the simultaneous annealing of cell parameters and internal coordinates effectively indexes the data during the process of structure solution.

Even though the single crystal data give an unambiguous structure for the LT phase, we can attempt a similar process

DOI: 10.1021/jacs.8b08591
J. Am. Chem. Soc. 2018, 140, 13441−13448

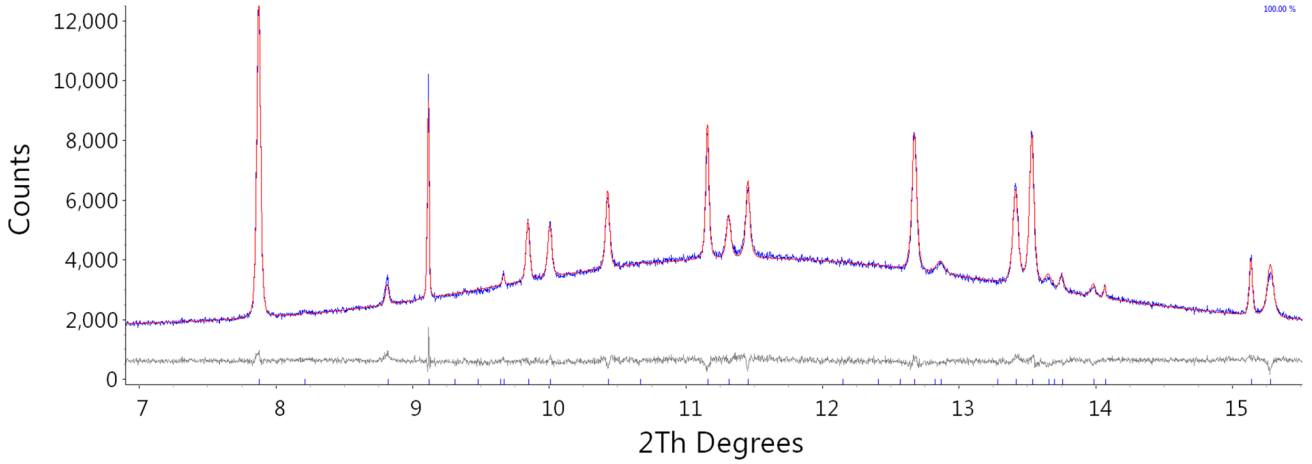

Figure 6. Fit of the #10 *Pc* candidate for the HT phase to 500 K synchrotron PXRD data.

Table 1. Refinement Results for HT Phase DC-MBI Cell Uses *P*11*b* Nonstandard Setting of *Pc* To Match Other Figures

Chemical formula	$C_6H_8Cl_2N_2$
Crystal system	Monoclinic
Space group	P11*b* (No. 7)
a (Å)	5.7702(1)
b (Å)	10.3934(2)
c (Å)	14.7421(3)
γ (deg)	91.2163(14)
V (Å^3)	884.01(3)
Z′	2
Temperature (K)	500
Wavelength (Å)	0.8257653
2θ range (deg)	5−30
Final $R_{wp}/R_p/R_{Bragg}$%	2.56/1.95/1.07

with powder data. With the higher quality LT data, the effect of *hkl*-dependent peak broadening is significant, and we find that in a *P*1 description the cell metric distorts slightly (90° angles are ±0.01) to describe this broadening, so that the quality of each candidate is dominated by the metric symmetry. If we use an orthorhombic cell metric for all candidates, we find that candidates #2 and #3 give essentially equivalent fits to the data with R_{wp} ∼ 0.15% higher than the *P*1 description. If we take the other extreme description and allow a triclinic cell metric for each candidate, candidate #3 is the best choice (ΔR_{wp} = 0.15%). This is the expected $Pca2_1$ candidate for the LT phase. A Rietveld fit to the LT data is included in Supporting Information (Figure S2).

Despite the relatively low information content of the laboratory VT-PXRD data, we can gain insight into the LT to HT transition from the temperature dependence of the rotational-mode amplitudes and corresponding molecular rotations discussed above (shown in Figure 7). On the basis of the group-subgroup relationships presented in Figure 4, we can use candidate #10 *Pc*, which has 6 allowed rotational modes (Γ_1^+, $2\Gamma_4^+$, $2\Gamma_2^-$, Γ_3^-) at all temperatures. Over the 150 data sets analyzed on warming and cooling, we find that R_{wp} increases by an average of 0.12% and a maximum of 0.25% if the $2\Gamma_2^-$ and Γ_3^- mode amplitudes are fixed at zero. The small R_{wp} increase and the absence of any noticeable temperature dependence suggest that these modes are unimportant and can be removed from the model. We see a clear increase in the Γ_4^+

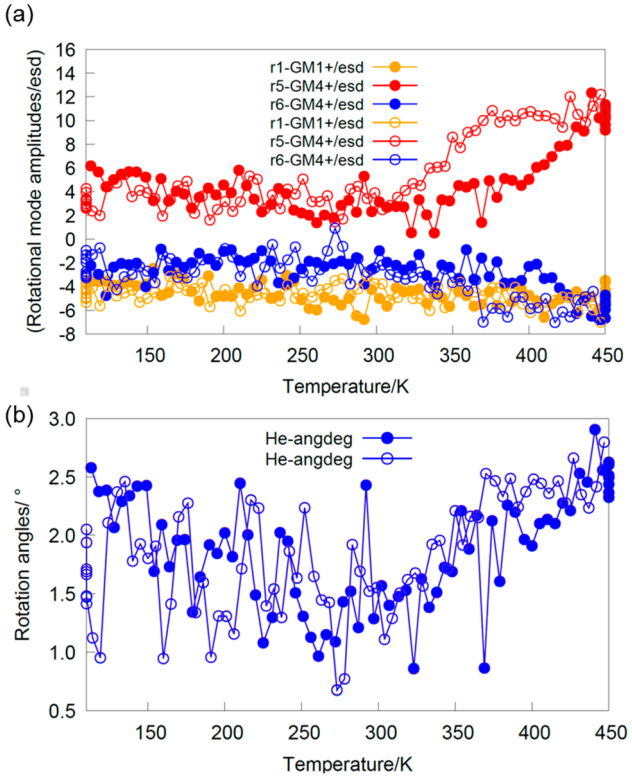

Figure 7. In both panels, closed circles indicate warming and open circles indicate cooling. (a) Important rotational-mode amplitudes/esd vs temperature, labeled according to parameter name and IR. (b) The overall molecular rotation angles for the two symmetry-unique molecules vs temperature. Observe the marked change in slope at the phase transition.

amplitudes and a marked decrease in their standard uncertainty above the phase transition temperature. We also find that the R_{wp} difference between a model in which rotational mode amplitudes are fixed at zero (the high symmetry $Pca2_1$ phase) and a model in which they are allowed to refine grows significantly at the phase transition.

Thermal Expansion of DC-MBI. The unit cell parameters of DC-MBI extracted from variable-temperature laboratory PXRD data by Rietveld refinement are plotted as a function of temperature in Figure 8. Below T_c (∼400 K), unit cell parameters expand smoothly upon warming, and show normal

DOI: 10.1021/jacs.8b08591
J. Am. Chem. Soc. 2018, 140, 13441−13448

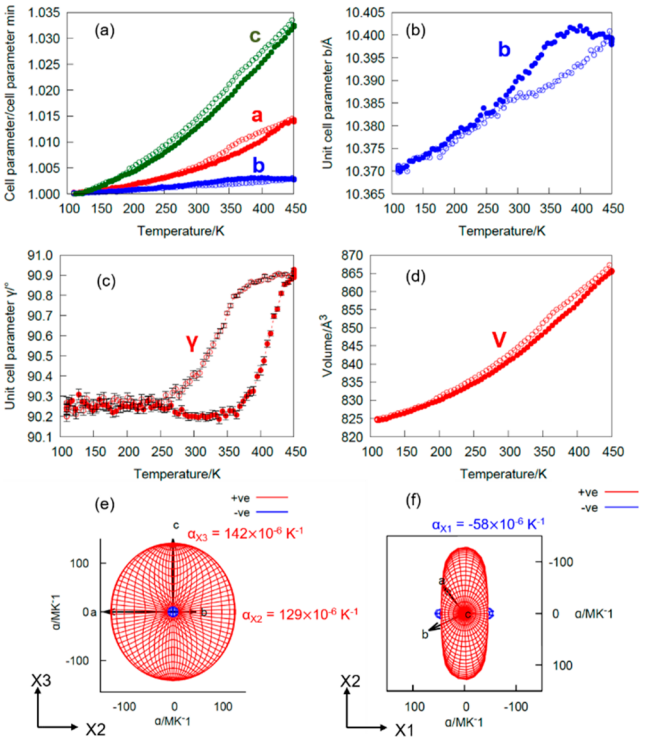

Figure 8. (a–c) Unit cell parameters and (d) cell volume from laboratory PXRD data vs temperature; in each panel closed circles indicate warming and open circles indicate cooling. Two views (e and f) of the thermal expansion indicatrix from 400 to 450 K; blue indicates negative thermal expansion and red indicates positive thermal expansion.

positive thermal expansion. At the phase transition to the monoclinic HT phase, cell parameters b and γ change rapidly. On cooling, cell parameters exhibit similar behavior, though the abrupt changes occur at a lower temperature ($T_c \sim 340$ K). This hysteresis suggests a first-order transition, which is consistent with the DSC results[41] reported in the literature and with our in situ heating experiments on single crystals. The calculated coefficients of linear thermal expansion (CTEs) are $\alpha_a = 108 \times 10^{-6}$ K^{-1}, $\alpha_b = 14.8 \times 10^{-6}$ K^{-1}, $\alpha_c = 36.3 \times 10^{-6}$ K^{-1} giving a volumetric coefficient α_v of 177×10^{-6} K^{-1} in the temperature range 100–500 K. The magnitude of α_a falls into the "colossal" expansion category ($|\alpha| > 100 \times 10^{-6}$ K^{-1}) observed in framework material such as $Ag_3[Co(CN)_6]$.[52]

Interestingly, the material contracts along the crystallographic b-axis over a ~50 K interval close to the phase transition temperature, showing uniaxial negative thermal expansion (NTE). This can be most clearly seen from the thermal expansion indicatrix, calculated using the PASCal[53] program and shown in Figures 8e,f and S3. The details of the principal axes and the CTE values along each principal axis are summarized in Tables S1 and S2. We observe a uniaxial NTE along the principal axis X_1 (close to b) and strong positive thermal expansion (PTE) along X_2 and X_3.

Discussion. Analysis of variable-temperature diffraction data, aided by the subgroup tree of Figure 4, gives a clear picture of the symmetry change that occurs at the LT–HT phase transition in DC-MBI. We consider first the relationship between the hypothetical *Pbcm* parent phase and the previously known LT phase. The small Γ_2^- rotational mode of the LT $Pca2_1$ structure breaks the *Pbcm* symmetry of the parent, but only slightly, so that it is best to consider the lower $Pca2_1$ symmetry as being derived principally from H3 ordering rather than from rotations. Starting from the H3-disordered *Pbcm* parent, we find that any pattern of H occupancies in the *P*1 base candidate #16 can be described using eight Γ-point occupational symmetry modes (modes that change site occupancy). In fact, the action of a single Γ_2^- occupancy mode produces the polar ordering pattern observed in the LT phase.

The low-symmetry HT phase (Figure 3b) is derived from the LT phase by the activation of primary Γ_4^+ rotational modes. In our model the two symmetry-allowed Γ_4^+ mode amplitudes have parameter names *r*5 and *r*6. If the amplitudes are related by $-r5 = +r6$, they describe equal rotations around the pseudo 2-fold axis of each molecule (the pink vector in Figure 1). This is essentially the rotation direction observed experimentally in HT-DCMBI (Figure 3b). The sensitivity of the rotation vector to the values of *r*5 and *r*6 can be appreciated by realizing that a change of sign of *r*5 such that $+r5 = +r6$ would rotate the vector by 90° until it lies approximately perpendicular to the molecular plane. The relatively large changes required in *r*5 and *r*6 to significantly change the direction of the rotation vectors give us confidence in the experimentally derived directions. The refined rotations (pink vectors in Figure 3b) lie essentially along the pseudo 2-fold axis of the molecules with alternate molecules along the H-bonded chains rotating in opposite directions. The other (secondary, small-magnitude) modes allowed by the symmetry of the HT structure ($2\Gamma_2^-$, Γ_3^-) rotate the molecule in the plane perpendicular to the chain direction and in the plane of the molecule, respectively (the blue vector in Figure 1 represents a pure Γ_3^- mode).

Perhaps the most unusual feature of the observed transition is that ferroelectric DC-MBI transforms from a higher-symmetry LT phase (orthorhombic polar) to a lower-symmetry HT phase (monoclinic polar) on heating. Most phase transitions are associated with an increase in symmetry on warming, though this is not a thermodynamic requirement. We see strong evidence from the hysteresis in the unit cell parameters and from the phase coexistence close to T_c that the LT↔HT transition in DC-MBI is discontinuous. It is accompanied by significant increases in a and c and a slight contraction in b.

There are a small number of examples of symmetry loss upon heating claimed in the literature on ferroelectric molecules, though several appear questionable on closer examination of the data and crystallographic analysis. In fact, the prototype ferroelectric Rochelle salt[54–58] undergoes a paraelectric–ferroelectric–paraelectric series of phase transitions on cooling or heating which involve a so-called "re-entrant" phase transition. The space group sequence is $P2_12_12$ ($T < 255$ K), $P2_111$ (255 K < T < 297 K) and $P2_12_12$ ($T > 297$ K. It is possible that DC-MBI would transition back to the $Pca2_1$ phase (or a *Pbcm* phase) at higher temperature, but it sublimes first.

The observation that DC-MBI transforms from polar space group $Pca2_1$ to polar space group *Pc* means that the phase transition does not provide a straightforward explanation for switching via a paraelectric high-symmetry structure, as proposed earlier. This is supported by SHG measurements which show the material remains noncentrosymmetric up to its melting point. The switching mechanism is therefore likely to involve nucleation and growth of chains with different H-

DOI: 10.1021/jacs.8b08591
J. Am. Chem. Soc. 2018, 140, 13441–13448

bonding directions. The lack of proton disorder in the HT phase also helps rationalize why the coercive field of DC-MBI was too high to measure a ferroelectric hysteresis loop at room temperature[41] and that switching could only be observed at elevated temperature.

CONCLUSIONS

In this paper, we describe the application of a novel symmetry-inspired methodology, based on rotational molecular symmetry modes, to understanding the behavior and to allow structure solution of the HT phase of an important organic functional material: the near-room-temperature molecular ferroelectric DC-MBI. This method allows us to exhaustively explore the possible symmetry-changing molecular rearrangements in this ferroelectric. We find that the HT phase has monoclinic *Pc* symmetry rather than the anticipated centrosymmetric orthorhombic *Pbcm* symmetry expected from simple crystallographic considerations. This is consistent with the retention of SHG activity all the way up to the material's sublimation point. The observation that DC-MBI undergoes a symmetry-reducing transition on warming is unusual. The phase transition appears to be first order and displays a ∼100 K hysteresis. Although ΔV_{trans} is positive, we observe a contraction of the *b*-axis close to the phase transition leading to uniaxial negative thermal expansion over a ∼50 K range.

This is the first example of using rotational symmetry-mode parameters and of systematic and exhaustive subgroup-tree exploration to solve an organic-molecule crystal structure. These methodologies have quite general importance, and will be widely applicable to fully molecular or molecular-fragment-containing functional materials such as MOFs and hybrid perovskites.

ASSOCIATED CONTENT

Supporting Information

The Supporting Information is available free of charge on the ACS Publications website at DOI: 10.1021/jacs.8b08591.

Data for $C_8H_6Cl_2N_2$ (CIF)

Symmetry data for $C_8H_6Cl_2N_2$ (CIF)

Rietveld fit of next best monoclinic structure; Rietveld fit of low-temperature structure; thermal expansion coefficients and expansivity indicatrix; unit cell parameters and rotational mode amplitudes obtained from different data sets and with different models (PDF)

AUTHOR INFORMATION

Corresponding Authors

*ivana.radosavljevic@durham.ac.uk

*john.evans@durham.ac.uk

ORCID

P. Shiv Halasyamani: 0000-0003-1787-1040

Ivana Radosavljevic Evans: 0000-0002-0325-7229

Notes

The authors declare no competing financial interest.

ACKNOWLEDGMENTS

B.J.C. acknowledges the US-UK Fulbright commission for a research fellowship and the University of Durham for hosting him on research leave during which part of this research was undertaken. We thank Diamond Light Source for access to beamline I11 that contributed to the results presented here. W.Z. and P.S.H. thank the Welch Foundation (Grant E-1457) and the NSF (DMR-1503573) for support.

REFERENCES

(1) Lines, M. E.; Glass, A. M. Applications Of Ferroelectrics. *Principles and Applications of Ferroelectrics and Related Materials*; Oxford University Press: Oxford, 2001.

(2) Bowen, C. R.; Kim, H. A.; Weaver, P. M.; Dunn, S. Piezoelectric and ferroelectric materials and structures for energy harvesting applications. *Energy Environ. Sci.* **2014**, *7* (1), 25−44.

(3) Megaw, H. Origin of ferroelectricity in barium titanate and other perovskite-type crystals. *Acta Crystallogr.* **1952**, *5* (6), 739−749.

(4) Kwei, G. H.; Lawson, A. C.; Billinge, S. J. L.; Cheong, S. W. Structures of the ferroelectric phases of barium titanate. *J. Phys. Chem.* **1993**, *97* (10), 2368−2377.

(5) Shirane, G.; Hoshino, S.; Suzuki, K. X-Ray Study of the Phase Transition in Lead Titanate. *Phys. Rev.* **1950**, *80* (6), 1105−1106.

(6) Shirane, G.; Axe, J. D.; Harada, J.; Remeika, J. P. Soft Ferroelectric Modes in Lead Titanate. *Phys. Rev. B* **1970**, *2* (1), 155−159.

(7) Xu, T.; Shimada, T.; Uratani, Y.; Wang, X.; Wang, J.; Kitamura, T. Multiferroic Phases and Transitions in Ferroelectric Lead Titanate Nanodots. *Sci. Rep.* **2017**, *7*, 45373.

(8) Bhide, V. G.; Hegde, M. S.; Deshmukh, K. G. Ferroelectric Properties of Lead Titanate. *J. Am. Ceram. Soc.* **1968**, *51* (10), 565−568.

(9) Gerson, R. Variation in Ferroelectric Characteristics of Lead Zirconate Titanate Ceramics Due to Minor Chemical Modifications. *J. Appl. Phys.* **1960**, *31* (1), 188−194.

(10) Clarke, R.; Glazer, A. M. Critical phenomena in ferroelectric crystals of lead zirconate titanate. *Ferroelectrics* **1976**, *14* (1), 695−697.

(11) Clarke, R.; Glazer, A. M. The ferroelectric-ferroelectric transition in rhombohedral lead zirconate-titanate. *Ferroelectrics* **1976**, *12* (1), 207−209.

(12) Chen, H. D.; Udayakumar, K. R.; Cross, L. E.; Bernstein, J. J.; Niles, L. C. Dielectric, ferroelectric, and piezoelectric properties of lead zirconate titanate thick films on silicon substrates. *J. Appl. Phys.* **1995**, *77* (7), 3349−3353.

(13) Busch, G.; Scherrer, P. Eine neue seignette-elektrische Substanz. *Naturwissenschaften* **1935**, *23* (43), 737−737.

(14) Slater, J. C. Theory of the Transition in KH_2PO_4. *J. Chem. Phys.* **1941**, *9* (1), 16−33.

(15) Tokunaga, M. Theory of Ferroelectric Phase Transition in KH_2PO_4 Type Crystals. IIDynamical Properties. *Prog. Theor. Phys.* **1966**, *36* (5), 857−874.

(16) Fukami, T. Refinement of the Crystal Structure of KH_2PO_4 in the Ferroelectric Phase. *physica status solidi (a)* **1990**, *117* (2), K93−K96.

(17) Koval, S.; Kohanoff, J.; Migoni, R. L.; Tosatti, E. Ferroelectricity and Isotope Effects in Hydrogen-Bonded KDP Crystals. *Phys. Rev. Lett.* **2002**, *89* (18), 187602.

(18) Koval, S.; Kohanoff, J.; Lasave, J.; Colizzi, G.; Migoni, R. L. First-principles study of ferroelectricity and isotope effects in H-bonded KH_2PO_4 crystals. *Phys. Rev. B: Condens. Matter Mater. Phys.* **2005**, *71* (18), 184102.

(19) Evans, I. R.; Howard, J. A. K.; Evans, J. S. O. Structural ferroelectric phase transition and polymorphism in 2-aminopyridine dihydrogen phosphate. *Cryst. Growth Des.* **2008**, *8* (5), 1635−1639.

(20) Yanovskii, V. K.; Voronkova, V. I. Ferroelectric Phase Transitions and Properties of Crystals of the KTiOPO4 Family. *physica status solidi (a)* **1986**, *93* (2), 665−668.

(21) Dahaoui, S.; Hansen, N. K.; Protas, J.; Krane, H.-G.; Fischer, K.; Marnier, G. Electric properties of $KTiOPO_4$ and $NaTiOPO_4$ from temperature-dependent X-ray diffraction. *J. Appl. Crystallogr.* **1999**, *32* (1), 1−10.

DOI: 10.1021/jacs.8b08591
J. Am. Chem. Soc. 2018, 140, 13441−13448

(22) Norberg, S. T.; Ishizawa, N. K-site splitting in $KTiOPO_4$ at room temperature. *Acta Crystallogr., Sect. C: Cryst. Struct. Commun.* **2005**, *61* (10), i99−i102.
(23) Yashima, M.; Komatsu, T. Order-disorder and displacive components in the ferroelectric-paraelectric phase transition of potassium titanyl phosphate $KTiOPO_4$. *Chem. Commun.* **2009**, No. 9, 1070−1072.
(24) Akhmatkhanov, A. R.; Vaskina, E. M.; Chuvakova, M. A.; Pelegova, E. V.; Shur, V. Y. Investigation of polarization reversal and analysis of switching current data in KTP single crystals. *Ferroelectrics* **2017**, *508* (1), 1−8.
(25) Valasek, J. Piezo-electric and allied phenomena in Rochelle salt. *Phys. Rev.* **1921**, *17* (4), 475−481.
(26) Valasek, J. Piezo-Electric Activity of Rochelle Salt under Various Conditions. *Phys. Rev.* **1922**, *19* (5), 478−491.
(27) Wieder, H. H. Ferroelectric Polarization Reversal in Rochelle Salt. *Phys. Rev.* **1958**, *110* (1), 29−36.
(28) Sandy, F.; Jones, R. V. Dielectric Relaxation of Rochelle Salt. *Phys. Rev.* **1968**, *168* (2), 481−493.
(29) Suzuki, E.; Shiozaki, Y. Ferroelectric displacement of atoms in Rochelle salt. *Phys. Rev. B: Condens. Matter Mater. Phys.* **1996**, *53* (9), 5217−5221.
(30) Sugano, R; Hirai, Y.; Tashiro, T.; Sekine, T.; Fukuda, K.; Kumaki, D.; Domingues dos Santos, F.; Miyabo, A.; Tokito, S. Ultrathin flexible memory devices based on organic ferroelectric transistors. *Jpn. J. Appl. Phys.* **2016**, *55* (10S), 10TA04.
(31) Gao, W.; Chang, L.; Ma, H.; You, L.; Yin, J.; Liu, J.; Liu, Z.; Wang, J.; Yuan, G. Flexible organic ferroelectric films with a large piezoelectric response. *NPG Asia Mater.* **2015**, *7*, e189.
(32) Owczarek, M.; Hujsak, K. A.; Ferris, D. P.; Prokofjevs, A.; Majerz, I.; Szklarz, P.; Zhang, H.; Sarjeant, A. A.; Stern, C. L.; Jakubas, R.; Hong, S.; Dravid, V. P.; Stoddart, J. F. Flexible ferroelectric organic crystals. *Nat. Commun.* **2016**, *7*, 13108.
(33) Jiang, X.; Lu, H.; Yin, Y.; Zhang, X.; Wang, X.; Yu, L.; Ahmadi, Z.; Costa, P. S.; DiChiara, A. D.; Cheng, X.; Gruverman, A.; Enders, A.; Xu, X. Room temperature ferroelectricity in continuous croconic acid thin films. *Appl. Phys. Lett.* **2016**, *109* (10), 102902.
(34) Horiuchi, S.; Ishii, F.; Kumai, R.; Okimoto, Y.; Tachibana, H.; Nagaosa, N.; Tokura, Y. Ferroelectricity near room temperature in co-crystals of nonpolar organic molecules. *Nat. Mater.* **2005**, *4*, 163−166.
(35) Horiuchi, S.; Kumai, R.; Tokura, Y. Room-temperature ferroelectricity and gigantic dielectric susceptibility on a supra-molecular architecture of phenazine and deuterated chloranilic acid. *J. Am. Chem. Soc.* **2005**, *127*, 5010−5011.
(36) Saito, K.; Amano, M.; Yamamura, Y.; Tojo, T.; Atake, T. Low-Temperature Phase Transitions of an Organic Ferroelectrics, Phenazine−Chloranilic Acid. *J. Phys. Soc. Jpn.* **2006**, *75* (3), 033601.
(37) Noohinejad, L.; Mondal, S.; Wölfel, A.; Ali, S. I.; Schönleber, A.; van Smaalen, S. Ferroelectricity of Phenazine−Chloranilic Acid at T = 100 K. *J. Chem. Crystallogr.* **2014**, *44* (8), 387−393.
(38) Day, C. A single-component organic crystal is ferroelectric at room temperature. *Phys. Today* **2010**, *63* (4), 16−17.
(39) Di Sante, D.; Stroppa, A.; Picozzi, S. Structural, electronic and ferroelectric properties of croconic acid crystal: a DFT study. *Phys. Chem. Chem. Phys.* **2012**, *14* (42), 14673−14681.
(40) Fernandez-Alonso, F.; Gutmann, M. J.; Mukhopadhyay, S.; Jochym, D. B.; Refson, K.; Jura, M.; Krzystyniak, M.; Jimenez-Ruiz, M.; Wagner, A. Hydrogen Bonding in the Organic Ferroelectric Croconic Acid: Insights from Experiment and First-Principles Modelling. *J. Phys. Soc. Jpn.* **2013**, *82*, SA001.
(41) Horiuchi, S.; Kagawa, F.; Hatahara, K.; Kobayashi, K.; Kumai, R.; Murakami, Y.; Tokura, Y. Above-room-temperature ferroelectricity and antiferroelectricity in benzimidazoles. *Nat. Commun.* **2012**, *3*, 1308.
(42) Muller, M.; Dinnebier, R. E.; Dippel, A.-C.; Stokes, H. T.; Campbell, B. J. A symmetry-mode description of rigid-body rotations in crystalline solids: a case study of $Mg(H_2O)_6RbBr_3$. *J. Appl. Crystallogr.* **2014**, *47* (2), 532−538.
(43) Coelho, A. A.; Evans, J. S. O.; Evans, I. R.; Kern, A.; Parsons, S. The TOPAS symbolic computation system. *Powder Diffr.* **2011**, *26* (4), S22.
(44) Coelho, A. TOPAS and TOPAS-Academic: an optimization program integrating computer algebra and crystallographic objects written in C. *J. Appl. Crystallogr.* **2018**, *51* (1), 210−218.
(45) Ok, K. M.; Chi, E. O.; Halasyamani, P. S. Bulk characterization methods for non-centrosymmetric materials: second-harmonic generation, piezoelectricity, pyroelectricity, and ferroelectricity. *Chem. Soc. Rev.* **2006**, *35* (8), 710−717.
(46) Lewis, J. W.; Payne, J. L.; Evans, I. R.; Stokes, H. T.; Campbell, B. J.; Evans, J. S. O. An Exhaustive Symmetry Approach to Structure Determination: Phase Transitions in $Bi_2Sn_2O_7$. *J. Am. Chem. Soc.* **2016**, *138* (25), 8031−8042.
(47) Campbell, B. J.; Stokes, H. T.; Tanner, D. E.; Hatch, D. M. ISODISPLACE: a web-based tool for exploring structural distortions. *J. Appl. Crystallogr.* **2006**, *39* (4), 607−614.
(48) Kerman, S.; Campbell, B. J.; Satyavarapu, K. K.; Stokes, H. T.; Perselli, F.; Evans, J. S. O. The superstructure determination of displacive distortions via symmetry-mode analysis. *Acta Crystallogr., Sect. A: Found. Crystallogr.* **2012**, *68* (2), 222−234.
(49) Campbell, B.; Evans, J.; Perselli, F.; Stokes, H. Rietveld refinement of structural distortion-mode amplitudes. *Ed Newsl* **2007**, *8*, 81.
(50) Stroppa, A.; Barone, P.; Jain, P.; Perez-Mato, J. M.; Picozzi, S. Hybrid Improper Ferroelectricity in a Multiferroic and Magneto-electric Metal-Organic Framework. *Adv. Mater.* **2013**, *25* (16), 2284−2290.
(51) Etter, M.; Müller, M.; Dinnebier, R. E. Rotational Rigid Body Symmetry Modes: A Tool for the Investigation of Phase Transitions. *Z. Anorg. Allg. Chem.* **2014**, *640* (15), 3079−3087.
(52) Goodwin, A. L.; Calleja, M.; Conterio, M. J.; Dove, M. T.; Evans, J. S. O.; Keen, D. A.; Peters, L.; Tucker, M. G. Colossal Positive and Negative Thermal Expansion in the Framework Material $Ag_3[Co(CN)_6]$. *Science* **2008**, *319* (5864), 794−797.
(53) Cliffe, M. J.; Goodwin, A. L. PASCal: a principal axis strain calculator for thermal expansion and compressibility determination. *J. Appl. Crystallogr.* **2012**, *45* (6), 1321−1329.
(54) Beevers, C. A.; Hughes, W. The Crystal Structure of Rochelle Salt (Sodium Potassium Tartrate Tetrahydrate $NaKC_4H_4O_6 \cdot 4H_2O$). *Proc. R. Soc. London, Ser. A* **1941**, *177* (969), 251−259.
(55) Solans, X.; Gonzalez-Silgo, C.; Ruiz-Pérez, C. A Structural Study on the Rochelle Salt. *J. Solid State Chem.* **1997**, *131* (2), 350−357.
(56) Gorbitz, C. H.; Sagstuen, E. Potassium sodium (2R,3R)-tartrate tetrahydrate: the paraelectric phase of Rochelle salt at 105 K. *Acta Crystallogr., Sect. E: Struct. Rep. Online* **2008**, *64* (4), m507−m508.
(57) Uddin, M. J.; Middya, T. R.; Chaudhuri, B. K. Room temperature ferroelectric effect and enhanced dielectric permittivity in Rochelle salt/PVA percolative composite films. *Curr. Appl. Phys.* **2013**, *13* (3), 461−466.
(58) Mo, F.; Mathiesen, R. H.; Beukes, J. A.; Vu, K. M. Rochelle salt − a structural reinvestigation with improved tools. I. The high-temperature paraelectric phase at 308 K. *IUCrJ* **2015**, *2* (Pt 1), 19−28.

DOI: 10.1021/jacs.8b08591
J. Am. Chem. Soc. 2018, 140, 13441−13448